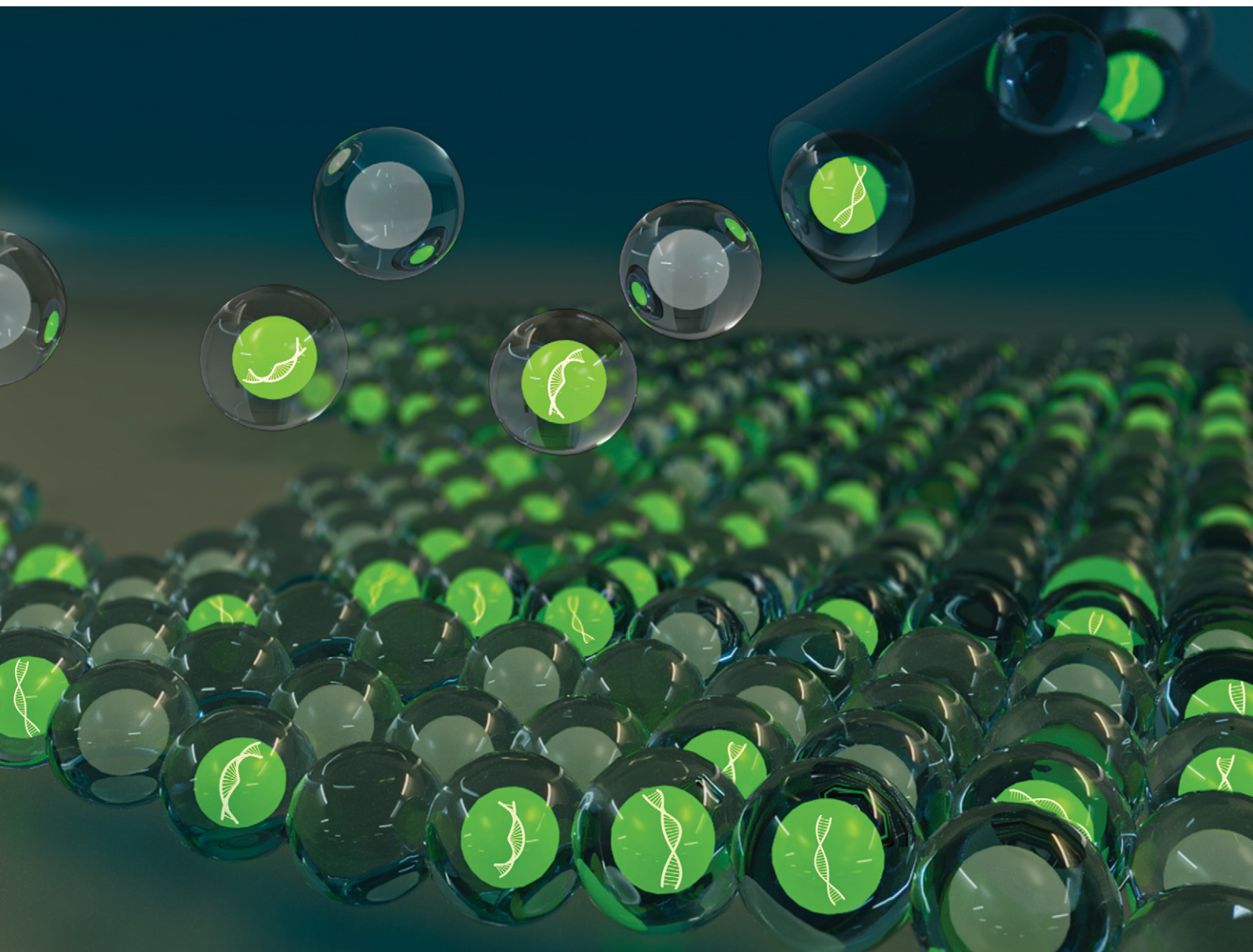


Lab on a Chip

Devices and applications at the micro- and nanoscale

rsc.li/loc



ISSN 1473-0197

PAPER

Nam-Trung Nguyen *et al.*
Precise, wide field, and low-cost imaging and analysis of
core-shell beads for digital polymerase chain reaction


 Cite this: *Lab Chip*, 2023, 23, 3353

Precise, wide field, and low-cost imaging and analysis of core–shell beads for digital polymerase chain reaction†

 Ajeet Singh Yadav, Fariba Malekpour Galogahi, Du Tuan Tran, Aditya Vashi, Chin Hong Ooi,  Kamalalayam Rajan Sreejith and Nam-Trung Nguyen *

Digital droplet reactors have become a valuable tool for the analysis of single cells, organisms, or molecules by discretising reagents into picolitre or nanolitre volumes. However, DNA-based assays typically require processing of samples on the scale of tens of microlitres, with the detection of as few as one or as many as a hundred thousand fragments. Through the present work, we introduce a flow-focusing microfluidic device that produces 120 picolitre core–shell beads, which are assembled into a monolayer in a Petri dish for visualization and analysis. The bead assembly is subjected to polymerase chain reaction (PCR) amplification and fluorescence detection to digitally quantify the DNA concentration of the sample. We use a low-cost 21-megapixel digital camera and macro lens to capture wide-field fluorescence images with a 10–30 mm² field-of-view at magnifications ranging from 5× to 2.5×. A customised Python script analysed the acquired images. Our study demonstrates the ability to perform digital PCR analysis of the entire bead assembly through end-point imaging and compare the results with those obtained through RT-qPCR.

 Received 18th April 2023,
Accepted 9th June 2023

DOI: 10.1039/d3lc00337j

rsc.li/loc

1 Introduction

Recently, there has been an increasing demand for molecular diagnostic tests that can detect and quantify specific DNA sequences.¹ Polymerase chain reaction (PCR) plays a fundamental role in diagnostic approaches, which are employed in a variety of applications including cancer² and foetal diagnostics,³ single cell studies,⁴ and analysis of genetically modified organisms.⁵ The first generation of detection involved endpoint analysis such as gel electrophoresis to obtain quantitative results.⁶ Second-generation systems were able to monitor amplification progression in real-time after each PCR cycle. This was achieved either by incorporating hydrolysis probes or intercalating dye. The DNA concentration was obtained from the cycle threshold (C_T), which is a point on the analogue fluorescence curve where the signal increases above background. However, imperfect amplification efficiencies could affect C_T values, limiting the accuracy of this technique for absolute quantitation.

The third generation of PCR involves digitisation of real-time PCR, which transforms the exponential, analogue

nature, and single molecular sensitivity of PCR into a linear, digital signal.^{7,8} In this approach, a dilution process isolates single molecules to be individually amplified by PCR, and the separate analysis of each product is carried out by partitioning the sample prior to PCR amplification. This division ensures that each reaction chamber contains either none or more than one copies of the target DNA sequence. The number of target DNA molecules present can be calculated from the fraction of positive end-point reactions using Poisson statistics.

Digital polymerase chain reaction (dPCR) methods are categorised based on sample partitioning methods such as division into droplets,⁹ microwells on chip,¹⁰ and microfluidics chambers.¹¹ In droplet-based digital PCR (ddPCR) sample passes through a microfluidic device to form segmented flow.¹² The sample is divided into tens of thousands of droplets separated by an immiscible liquid, such as mineral oil forming an emulsion. Alternatively, in the case of chip-based digital PCR (cdPCR) sample is loaded into a silicon chip with micromachined wells. Following thermal cycling, the chip is imaged by fluorescence microscopy to determine the number of wells with positive PCR results.

Our system follows a workflow that resembles a conventional ddPCR setup, but employing several flow focusing configurations to generate core–shell droplets.¹³ The microfluidic system is a droplet generator without an integrated thermocycler. We generated double emulsion as

Queensland Micro- and Nanotechnology Centre, Griffith University, 170 Kessels Road, Nathan, QLD 4111, Australia. E-mail: nam-trung.nguyen@griffith.edu.au

† Electronic supplementary information (ESI) available. See DOI: <https://doi.org/10.1039/d3lc00337j>

opposed to conventional single emulsion. Curing the outer layer of the double emulsion into a solid shell facilitates minimum cross-contamination. Conventional ddPCR was often integrated with capillary tubes to analyse the droplets in continuous manner.^{14,15} These modifications were adopted to minimize contamination caused by manual handling or cross-contamination due to coalescence. However, the workflow of such systems is complicated, requiring high pressure systems to maintain uniform pressure in longer capillary tubes, continuous-flow thermocycling and suffers from low throughput due to sequential detection. More importantly, ddPCR is plagued with coalescence of droplets during the thermocycling process. This necessitates the use of surfactants, which may interfere with PCR amplification and detection.¹⁶ On the other hand, cross-contamination of the samples in cdPCR is difficult to eliminate due to its workflow.¹⁷ In a typical cdPCR sample filling process, the sample is directed sequentially to each compartment unit. Subsequently, the samples outside of the microchambers are removed, and the units are sealed. However, the removal of excess sample is often not completely thorough, resulting in the presence of sample residue. This residue can potentially cause cross-contamination between microchambers.¹⁷

The PCR samples can also be distributed in the form of core-shell liquid beads. The sample containing liquid core is encapsulated by a polymeric shell. Such core-shell structure isolates the PCR samples from external environment thus minimising contamination. The robust polymer shell ensures easy handling and safeguards against physical rupturing.¹⁸ These features enable long term storage of the samples. Following the PCR process, the samples can also be retrieved for further analysis.¹⁹ Core-shell beads produced by droplet-based microfluidics offer excellent control over the size of the core and thickness of the shell of the liquid bead. The core precisely meters and confines the volume of reactions; thus, its size uniformity ensures the accuracy of quantitative results. Moreover, core-shell beads remain stable without merging during thermocycling.¹⁸

The present work describes the use of core-shell beads as microchambers for dPCR and showcases a cost-effective, wide-field imaging technique for its evaluation. We report an image analysis method for liquid beads which eliminates the need for corrections related to lens distortion, skewness, or non-uniform illumination. Moreover, the detection efficiency based on shape remains unaffected by the arrangement of the beads.²⁰ The presented dual light setup is crucial in detecting beads with or without cores contributes to the high dPCR accuracy. Our imaging setup utilises a commercial-grade digital single lens reflex (dSLR) camera and filters, rendering an expensive microscope unnecessary. We developed the image analysis algorithm using Python on a freely available text editor. Apart from the setup cost, the running cost of the PCR process only include reagents, and chemicals required to generate core-shell beads. It is worth noting that each reaction chamber necessitates only a volume close to 100 picolitres, resulting in a considerable reduction

in reagent costs. In contrast to a conventional flow focusing ddPCR device, our microfluidic device was designed for the generation of double emulsion with a surface treatment, curing of shell layer. A flow-focusing microfluidic device uses trimethylolpropane trimethacrylate (TMPTMA) as shell phase and water as core phase. The properties of TMPTMA such as its transparency,²¹ thermal stability,¹⁸ non-toxicity,²² and biocompatibility,²³ make it highly suitable for PCR applications. Our image acquisition setup consists of a 21-megapixel dSLR camera equipped with a 25 mm macro-lens at 2.5× to 5× magnification for capturing an area of 20 mm². We employed a camera-mounted two-axis scanning platform to capture the entire assembly of produced beads. For each section of the bead assembly, two images are captured, one in fluorescent mode and the other in brightfield mode. The number of beads with and without cores is detected and counted using a simple circle detection-based image analysis of brightfield images. The fluorescent and non-fluorescent cores are separated using pixel value and size thresholding. The results demonstrate the promising proof of concept of utilising liquid beads for dPCR.

2 Materials and methods

2.1 Preparation of core-shell beads

Fig. 1 illustrates the flow-focusing geometry utilised in producing core-shell droplets. This device is comprised of three flow-focusing junctions, as well as various inlets and an outlet. Inlet 1 introduces the dispersed phase, inlet 2 is for the shell phase, inlets 3 and 4 are for the continuous phase, and inlet 5 is for the spacer phase. All channels have a uniform depth of 120 μm and a width of 100 μm, except the 30 μm constriction for the formation of sample droplets. The channels were chemically modified to with a hydrophilic section and a hydrophobic section to facilitate the generation of core-shell droplets, Fig. 1. To make the channel surfaces hydrophilic, a 1 wt% polyvinyl acetate (PVA) solution was manually introduced. The hydrophobic sections of channels were prevented from being coated with PVA by simultaneously injecting air. The PVA solution was removed, and the device was annealed at 100 °C for 15 minutes. This process was repeated three times. Subsequently, the remaining section of the channel was made hydrophobic using Aquapel. Using the same technique for PVA coating, air was injected to block Aquapel from reaching the hydrophilic sections. Finally, Aquapel was completely removed by blowing air.

To create the core-shell droplets, the core phase is introduced through the first inlet and intersects with the shell phase flowing through the second inlet at the first junction. The core droplets are then encapsulated by the shell phase at the second junction. At this point, the continuous phase is introduced through the third and fourth inlets to disperse the shell phase. The core-shell droplets then move on to the third junction, where the spacer phase is added to prevent coalescence. The core-shell droplets exit

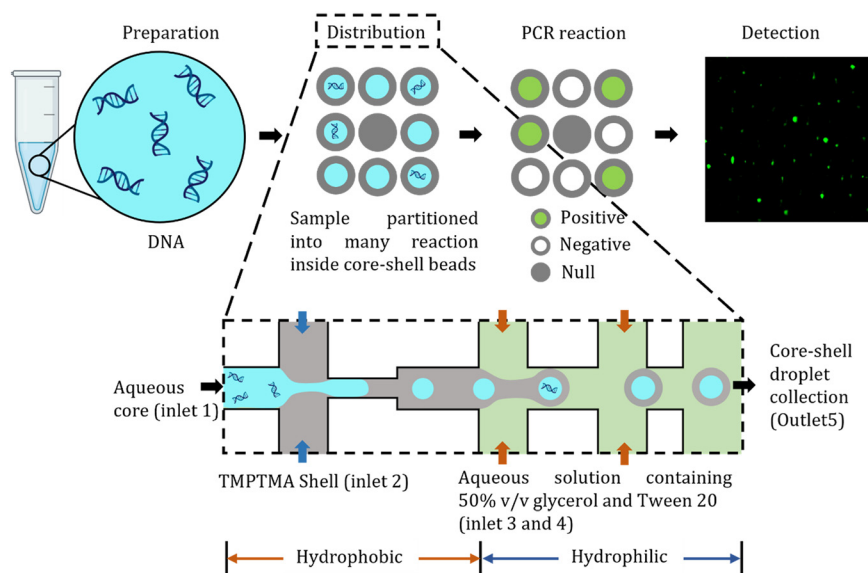


Fig. 1 Schematics illustrates workflow of the dPCR process, starting from preparation to detection. We employed core-shell beads for compartmenting initial bulk DNA samples, which were produced using microfluidics, ESI† Video S1.

the device through the outlet to be collected in a Petri dish. Following the collection, the formed core-shell droplets are exposed to a 24 W blue light (450–490 nm) source for 20 minutes to polymerize and form liquid beads, solid particles with a liquid core.²⁴ However, the throughput is lower than conventional ddPCR methods.²⁵ This is attributed to slower optimised flow rate and about 50% of the produced beads are core-shell.

2.2 PCR

2.2.1 Reagents. The AllBac primers (*Bacteroides* species, Thermo Fisher Scientific) were utilised to detect *Bacteroidales* 16S rRNA genes (accession number AY597127) from DNA extracts obtained from the fecal sample of a healthy individual using the QIAamp DNA stool mini kit (Qiagen). Three independent serial dilutions of DNA were tested to determine the sensitivity of the analyses. The 20 μL PCR mixture consisted of 15 pmol of the primers AllBac296F and AllBac467R, 10 μL SYBR Green Supermix mix, 2 μL of DNA with concentrations of 37.88 $\text{ng } \mu\text{L}^{-1}$, 18.94 $\text{ng } \mu\text{L}^{-1}$, 9.47 $\text{ng } \mu\text{L}^{-1}$, and 0.947 $\text{ng } \mu\text{L}^{-1}$, as well as 4 μL of DNase-free water to reach the desired volume. All components were thoroughly mixed prior to encapsulation.

2.2.2 RT-qPCR. To perform RT-qPCR analysis, a 20 μL mixture was prepared. The mixture contained 10 μL of Supermix, 2 μL of forward and reverse primer, 2 μL of template DNA (9.47 $\text{ng } \mu\text{L}^{-1}$), and 4 μL of nuclease-free water. SYBR Green Supermix PCR was used for the analysis with the following thermal cycle conditions: an initial activation step for 10 min at 95 $^{\circ}\text{C}$, followed by 40 cycles of denaturation for 30 s at 95 $^{\circ}\text{C}$, annealing for 60 s at 53 $^{\circ}\text{C}$, and extension for 60 s at 60 $^{\circ}\text{C}$. Serial dilution of the initial template DNA sample results in sample with concentration ranging from

13 980 000 copies per reaction to 1.398 copies per reaction. Triplicate reactions were performed for all samples, including a negative control without DNA.

2.2.3 dPCR. To encapsulate the PCR mixture, we introduced the mixture as a core phase from the first inlet using a syringe pump. We used TMPTMA and the mixture of 50% v/v glycerol and $10^{-3} \text{ mol L}^{-1}$ Tween 20 as the shell phase and the continuous and spacer phase, respectively. The flow rates of the core, shell, continuous, and spacer phases were 10 $\mu\text{L h}^{-1}$, 100 $\mu\text{L h}^{-1}$, 200 $\mu\text{L h}^{-1}$, and 200 $\mu\text{L h}^{-1}$, respectively. The liquid beads obtained from this process were collected in PCR tubes. The collected samples were subsequently moved to thermal cycling. PCR cycling conditions were 95 $^{\circ}\text{C}$ for 10 min, followed by 40 cycles of 95 $^{\circ}\text{C}$ for 30 s, 53 $^{\circ}\text{C}$ for 60 s, and 60 $^{\circ}\text{C}$ for 60 s, performed in a conventional thermocycler (Bio-Rad CFX Connect, NSW, Australia).

Once the thermal cycling was completed, the liquid beads were moved to a pre-filled Petri dish containing water. To prevent bead agglomeration, the Petri dish was shaken gently, while a slight tilt allowed the beads to settle into a monolayer. Such configuration of beads with minimal agglomeration is optimal for accurate imaging and analysis. The imaging setup, Fig. 2, captured both bright field and fluorescent images. The fluorescent images were analysed using ImageJ to count the number of positive cores, while a custom Python code was employed to count all cores and beads. Subsequently, the concentration of the target DNA was determined using the Poisson distribution.

2.3 Scanning setup

The experimental setup comprised of a manual lab jack with a mounted motorized 2-dimensional stage, Fig. 2.

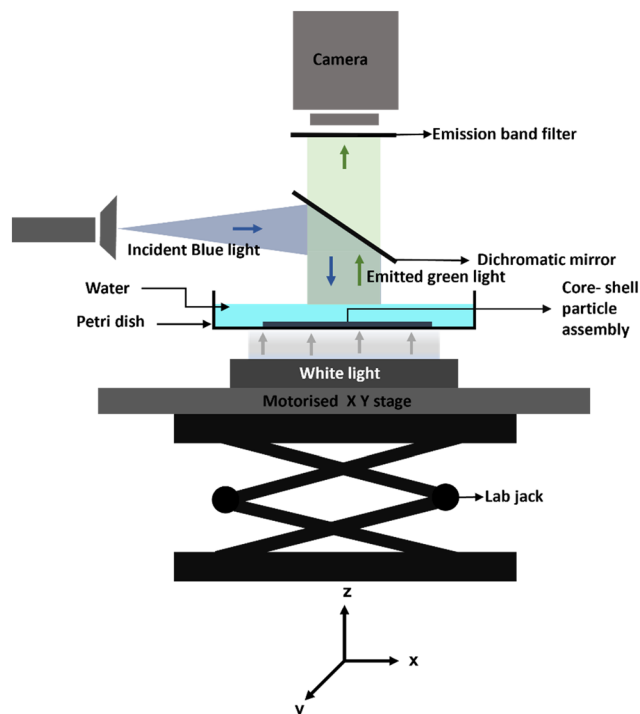


Fig. 2 A movable imaging and scanning setup for digital PCR (dPCR) consisting of a 3-axis system with a white and blue light source, fluorescence filter set, lens, and dSLR camera.

The lab jack provides movement in the z direction, while the x - y stage is created by integrating two linear stepper motors perpendicular to one another. This arrangement allows for three linear degrees of freedom along the x , y , and z axes. The vertical motion is necessary to focus the samples, as the camera and lens setup is optimized for a fixed magnification. To achieve focus, the camera or sample must be moved relative to one another. Keeping in mind the high susceptibility of the micro beads to go out of focus, only sample stage was made movable. The x - y stage is required to image

the entire assembly, as the field of view at $2.5\times$ magnification has an area of 30 mm^2 , which is much smaller than the size of the bead assembly. The light sources and samples are mounted on the stage, while the camera remains fixed and set to view from the top. The stepper motors' motion is calibrated to cover the entire assembly section with minimal overlap.

2.4 Bright-field and fluorescent imaging

Wide-field fluorescence imaging allows for viewing an area of 20 mm^2 in a single image acquisition process. Both optical setup and a high-resolution imaging setup were required to adequately resolve about 5000 beads. Fig. 3(A) depicts size distribution of beads in such an assembly. Images with a large field of view were captured using a Nikon D7500 dSLR camera with a 21-megapixel CMOS sensor and a 25 mm $f/2.8$ Macro Lens (Laowa 2.5–5 \times Ultra Macro), Fig. 3(B). The camera and lens were mounted on a tripod and positioned above the Petri dish containing beads. The source of white light was a 13 W RGB LED light panel. Fluorescence imaging ability was added using a blue flashlight torch and a series of filters and mirrors (GFP 25 mm Nikon, Japan). Excitation bandpass filter having a wavelength range of 450–490 nm, dichromatic mirror with cut-on wavelength 500 nm and emission filter with cut-on wavelength 515 nm were used. Excitation filter was placed 25–50 mm above and perpendicular to Petri dish allowing blue light to reach the dichroic mirror. The mirror is placed at 45° above the Petri dish to illuminate the sample from top. The 25 mm emission filter was positioned on the front of the lens. The setup is capable of imaging 10–30 mm^2 at $5\times$ to $2.5\times$ magnification, respectively. Image capture settings were typically taken at $f/2.8$ aperture, ISO 100–200, $2.5\times$ magnification, 5 cm working distance, and 2–10 s exposure in RAW image format. With these imaging parameters, resolution of 4000 pixels per bead and 800 pixels per core could be achieved.

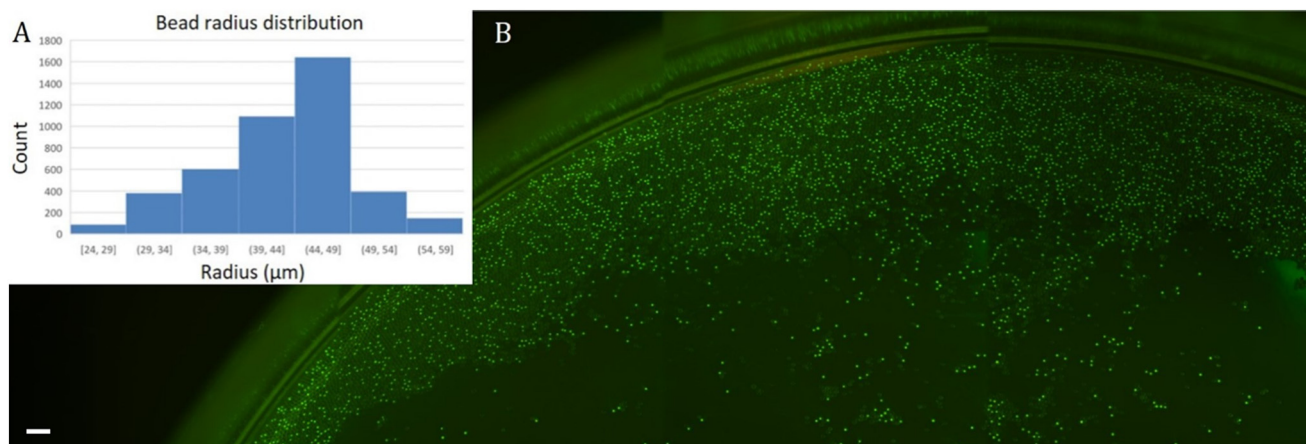


Fig. 3 Liquid beads for dPCR: (A) bead size distribution; (B) wide field high-resolution fluorescent image of beads assembly created by stitching 8 individual images. Scale bar is $500\text{ }\mu\text{m}$.

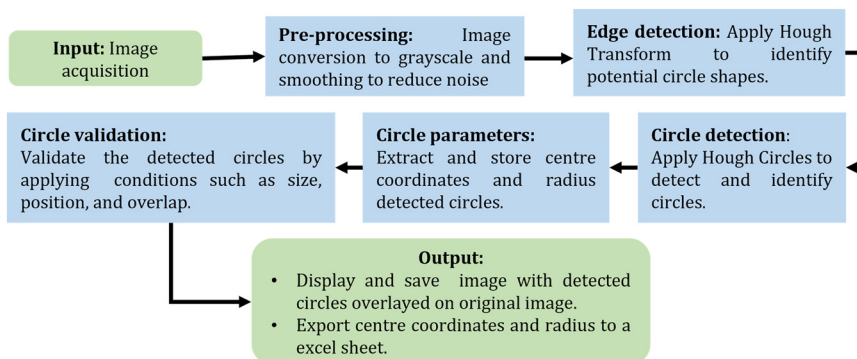


Fig. 4 Flow chart of the detection algorithm for circles in an image using OpenCV library in python.

3 Result and discussions

3.1 Analysis of bright field and fluorescent images

The imaging setup and analysis method was first calibrated using water diluted fluorescent dye as the core phase. The microfluidic method to generate core-shell beads have limitations as a fraction of the produced beads did not have cores in them. We analysed the bright field images to ascertain the presence of cores. Near circular shapes of beads and cores motivated us to utilise circle detection methods. Hough circle transform²⁶ (HCT) was inducted in custom made python script to detect beads with and without cores. Fig. 4 explains the algorithm of the image processing script in the form of a flow chart. We employed ImageJ to detect

the fluorescent cores. The acquired images had a high signal-to-noise ratio, which made it easy to identify the cores. The process involved two stages: pixel value thresholding and pixel size thresholding. The first stage separated the signal from the background, and the second stage eliminated pixel clusters smaller than the size of the core. The algorithm took about 20 s to analyse the stitched images.

3.2 Detection accuracy

We validated the analysis accuracy by randomly selecting smaller sections of the full image and examining the beads individually. Each bead is checked for presence of core in the brightfield image. Each core is checked for

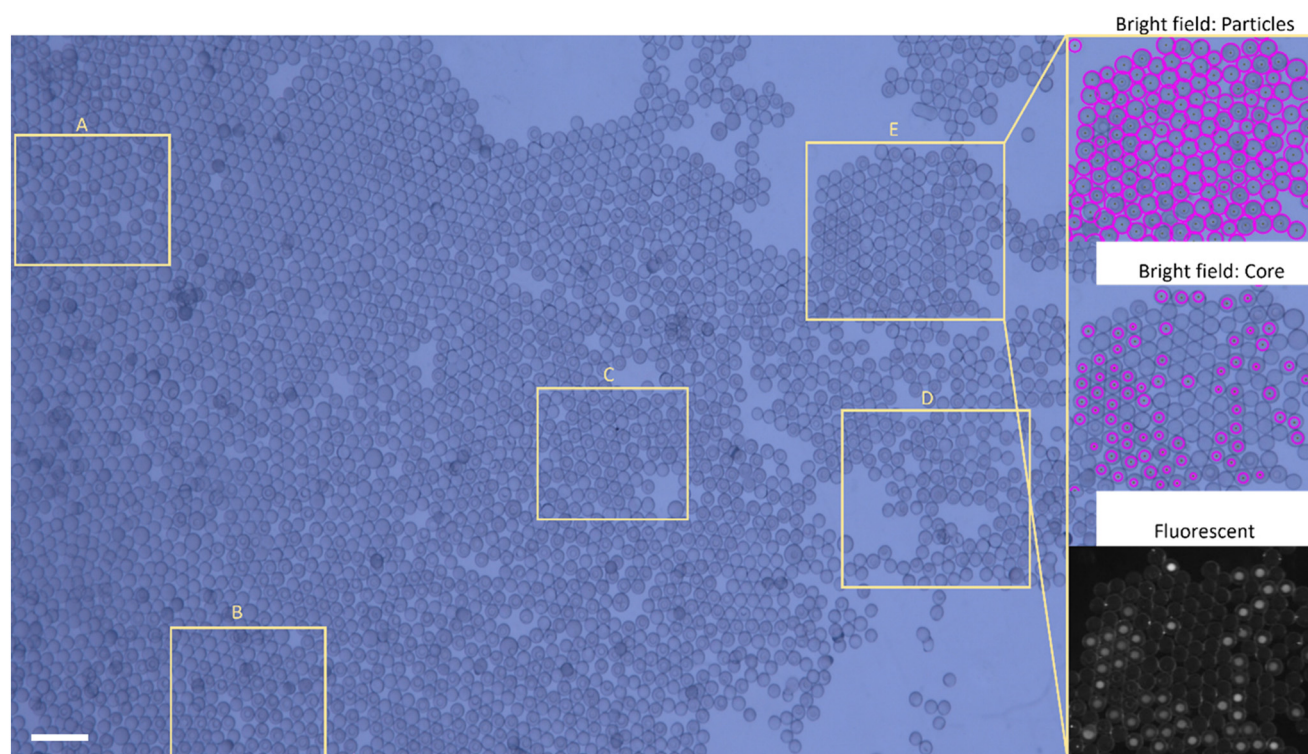


Fig. 5 Smaller region of brightfield and fluorescent images are analysed for detection accuracy, yellow boxes enclose regions A to E. Detected positives, negatives and null beads are shown for region E. Top and middle insets show detected beads and cores encircled in magenta colour. Scale bar is 500 μm .

Table 1 Representative error in detection of core, beads and fluorescence for various regions of acquired image, Fig. 5

Region	Beads		Core		Fluorescence	
	Total count	% error	Total count	% error	Total count	% error
A	111	3.6	33	6.3	27	1.8
B	101	2.9	59	5.8	35	1.9
C	84	3.5	60	5.9	40	2.3
D	123	4.8	68	8.1	61	4
E	149	4.6	59	7.3	50	3.3

signals in the fluorescent image, Fig. 5. The beads were divided into three categories for easier analysis; (i) null: bead without core; (ii) negative: core-shell bead without fluorescent; (iii) positive: core-shell bead with fluorescence. To accurately identify and quantify these three types of beads, we implemented a categorization approach. Using the Hough circle transform, larger circles were identified and counted as beads (Fig. 5, top inset). The smaller circles within these detected larger circles were counted as cores (Fig. 5, middle inset). The number of null beads was determined by subtracting the number of cores from the total number of beads. To determine the number of positive beads, we employed pixel value thresholding and pixel size thresholding techniques (Fig. 5, bottom inset). The number of negative beads was calculated by subtracting the number of positive beads from the total number of cores, representing the core-shell beads that did not exhibit fluorescence. Table 1 lists the representative misdetection of beads, cores, and fluorescence for each region.

3.3 Digital PCR quantification

At first, we conducted RT-qPCR on a dilution of $9.47 \text{ ng } \mu\text{L}^{-1}$ to evaluate the PCR mixture and compare the outcomes to dPCR results, ESI† Fig. S1. The RT-qPCR analysis estimated 1677 copies of DNA per microlitre (μL) of reaction mix. For dPCR, we employed microfluidics to produce core-shell beads that contain the DNA samples. The DNA solution was encapsulated into numerous monodispersed core-shell beads, with a fraction of beads remaining coreless (null). The beads underwent PCR thermocycling. According to previous studies, cores with one or more copies of the DNA emit distinctive fluorescent signals compared to those without DNA. However, we observed that most cores displayed fluorescence at a DNA concentration of $94.7 \text{ ng } \mu\text{L}^{-1}$. Upon image analysis, we noticed an overestimation of DNA concentration by about twice the actual value. Consequently, we decided to work with sequentially diluted concentrations of 5 \times , 10 \times , and 100 \times of the initial concentration. To confirm the specificity of the dPCR, we employed liquid beads without a DNA template as a negative control. For each experimental run, we randomly selected thousands of core-shell beads and captured both brightfield and fluorescent images. The images were analysed to determine the number of positives, negatives, and null entities. Finally, we estimated the DNA concentration using Poisson statistics, eqn (1).

$$(n, \lambda) = \frac{\lambda^n e^{-\lambda}}{n!}, \lambda = 0, 1, 2, \dots \quad (1)$$

where n represent the number of DNA molecules per microchamber, and λ denote the ratio of the total number of target DNA molecules to the number of reaction chambers *i.e.*, cores. If a core exhibits an increase in fluorescent signal, it indicates the presence of at least one target molecule within that core. Consequently, the probability of a core containing at least one target DNA template, denoted by f_0 , is equal to the ratio between fluorescent cores and the total number of cores. Thus:

$$f_0 = P(n > 0, \lambda) = 1 - P(n = 0, \lambda) = 1 - e^{-\lambda} \quad (2)$$

$$-\ln(1 - f_0) = \lambda \quad (3)$$

$$C_0 = \frac{\lambda}{V_{\text{core}}} \quad (4)$$

where C_0 is the DNA concentration and the average core volume V_{core} is $2 \times 10^{-4} \mu\text{L}$.

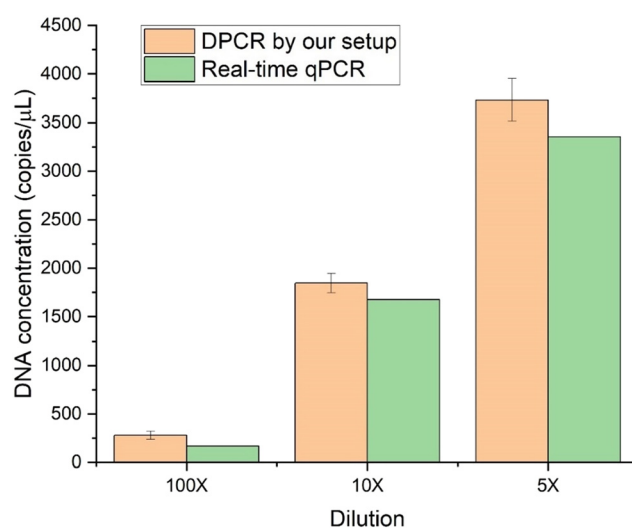


Fig. 6 Comparison of quantification results for 16S rRNA gene fragment detection using our device's endpoint dPCR and conventional RT-qPCR system. The analysis involved three different concentrations of 1677 copies per μL , 1677 copies per μL , and 3354 copies per μL .

Fig. 6 compares the performance of our endpoint dPCR detection setup with RT-qPCR system.

4 Conclusion

This paper presents a dual light imaging approach for analysing core-shell beads for digital PCR. The setup includes a dSLR camera mounted scanning device that captures high-resolution images of the bead assembly, enabling precise endpoint detection of positive, negative, and null beads. The core-shell beads are synthesized using a flow focusing microfluidic device, with the core containing DNA dilutions. The transparent shell allows for the detection of fluorescent signals and reduces cross-contamination. The stable shell structure prevents coalescence during thermocycling as well as evaporation,²⁷ leading to efficient amplification. The results obtained from the digital PCR assay were compared with those from the RT-qPCR assay, indicating a good agreement in terms of efficiency and quantification.

Compared to conventional ddPCR method, our approach with core-shell beads has several advantages. In ddPCR, amplification occurs in a customised thermocycler, while our method works with any commercial PCR equipment. Although both approaches allow for amplification and analysis, ddPCR typically has a lower detection limit, ranging from 500 to 100 000 copies per mL. We have not determined the specific detection limit for core-shell beads in this study. The present data demonstrate that our approach can detect approximately 28 000 copies per mL. Hatch *et al.* reported a reaction volume of 50 pL, which is significantly smaller than commercially available ddPCR systems like Bio-Rad QX200™.²⁵ The current minimum volume of our core-shell beads is 120 pL. Conventional ddPCR systems can achieve a throughput up to 50 times higher than our method. However, the analysis of a large number of droplets in ddPCR is time-consuming due to the sequential nature of this process, requiring 2.5–3 hours for statistically significant results. Our method currently needs 3.5–4 hours for processing approximately 25 000 beads. Regarding cost, the operational cost of continuous flow ddPCR is relatively high due to the requirement of a high-pressure system, a continuous-flow thermocycler, and the use of lasers for illumination or detection. Commercial ddPCR systems also require significantly higher reagent volumes, further contributing to the overall cost. In our method, we utilize an imaging system with a commercial-grade DSLR camera and filters, eliminating the need for an expensive microscope. The image analysis algorithm is developed based on open source platforms, reducing costs associated with proprietary software.

Author contributions

A. S. Y.: experiment, validation, writing – original draft. F. M. G.: experiments and review (supporting). D. T. T.: writing and

review (supporting). A. V.: writing and review (supporting). K. R. S.: review and supervision (supporting). C. H. O.: conceptualization and review (supporting). N.-T. N.: conceptualization, review, editing and supervision (lead).

Conflicts of interest

The authors have no conflicts to disclose.

Acknowledgements

N. T. N. acknowledges funding support from the Australian Research Council (ARC) through the ARC Discovery Project DP220100261. This work was partly performed at the Queensland node at Griffith University of the Australian National Fabrication Facility, a company established under the National Collaborative Research Infrastructure Strategy to provide nano and microfabrication facilities for Australian researchers. A. S. Y., F. M. G., D. T. T. and A. V. acknowledge funding support from the Griffith University International Postgraduate Research Scholarship and an ARC Postgraduate Research Scholarship.

References

- 1 R. Sanders, J. F. Huggett, C. A. Bushell, S. Cowen, D. J. Scott and C. A. Foy, *Anal. Chem.*, 2011, **83**, 6474–6484.
- 2 B. Vogelstein and K. W. Kinzler, *Proc. Natl. Acad. Sci. U. S. A.*, 1999, **96**, 9236–9241.
- 3 H. C. Fan and S. R. Quake, *Anal. Chem.*, 2007, **79**, 7576–7579.
- 4 E. A. Ottesen, J. W. Hong, S. R. Quake and J. R. Leadbetter, *Science*, 2006, **314**, 1464–1467.
- 5 M. J. Burns, A. M. Burrell and C. A. Foy, *Eur. Food Res. Technol.*, 2010, **231**, 353–362.
- 6 H. Zhu, H. Zhang, Y. Xu, S. Laššáková, M. Korabečná and P. Neuzil, *BioTechniques*, 2020, **69**, 317–325.
- 7 S. Zhou, T. Gou, J. Hu, W. Wu, X. Ding, W. Fang, Z. Hu and Y. Mu, *Biosens. Bioelectron.*, 2019, **128**, 151–158.
- 8 Z. Yan, H. Zhang, X. Wang, M. Gaňová, T. Lednický, H. Zhu, X. Liu, M. Korabečná, H. Chang and P. Neuzil, *Lab Chip*, 2022, **22**, 1333–1343.
- 9 P.-L. Quan, M. Sauzade and E. Brouzes, *Sensors*, 2018, **18**, 1271.
- 10 H. Shao, J. Chung, K. Lee, L. Balaj, C. Min, B. S. Carter, F. H. Hochberg, X. O. Breakefield, H. Lee and R. Weissleder, *Nat. Commun.*, 2015, **6**, 6999.
- 11 Y. Fu, H. Zhou, C. Jia, F. Jing, Q. Jin, J. Zhao and G. Li, *Sens. Actuators, B*, 2017, **245**, 414–422.
- 12 J. Sivasamy, T.-N. Wong, N.-T. Nguyen and L. T.-H. Kao, *Microfluid. Nanofluid.*, 2011, **11**, 1–10.
- 13 A. A. Kojabad, M. Farzanehpour, H. E. G. Galeh, R. Dorostkar, A. Jafarpour, M. Bolandian and M. M. Nodooshan, *J. Med. Virol.*, 2021, **93**, 4182–4197.
- 14 J. Chen, Z. Luo, L. Li, J. He, L. Li, J. Zhu, P. Wu and L. He, *Lab Chip*, 2018, **18**, 412–421.
- 15 A. C. Hatch, T. Ray, K. Lintecum and C. Youngbull, *Lab Chip*, 2014, **14**, 562–568.

- 16 G. Etienne, A. Vian, M. Biočanin, B. Deplancke and E. Amstad, *Lab Chip*, 2018, **18**, 3903–3912.
- 17 J. Li, Y. Qiu, Z. Zhang, C. Li, S. Li, W. Zhang, Z. Guo, J. Yao and L. Zhou, *Analyst*, 2020, **145**, 3116–3124.
- 18 F. M. Galogahi, A. Ansari, A. J. T. Teo, H. Cha, H. An and N.-T. Nguyen, *Biomed. Microdevices*, 2022, **24**, 40.
- 19 W. Liu, Y. Zhu and F. Stellacci, *ACS Sustainable Chem. Eng.*, 2023, **11**, 5524–5536.
- 20 Z. Yan, H. Zhang, X. Wang, M. Gaňová, T. Lednický, H. Zhu, X. Liu, M. Korabečná, H. Chang and P. Neuzil, *Lab Chip*, 2022, **22**, 1333–1343.
- 21 D. Chen, Y. Yao, Y. Wang, Y. Fu, J. Zheng and H. Zhou, *J. Mater. Chem. C*, 2020, **8**, 2993–2999.
- 22 X. Gu, H. Sun, X. Kong, C. Fu, H. Yu, J. Li and J. Wang, *Colloid Polym. Sci.*, 2013, **291**, 1771–1779.
- 23 S. Ghasaban, M. Atai, M. Imani, M. Zandi and M.-A. Shokrgozar, *J. Biomed. Mater. Res., Part A*, 2011, **99A**, 240–248.
- 24 F. M. Galogahi, M. Christie, A. S. Yadav, H. An, H. Stratton and N.-T. Nguyen, unpublished work.
- 25 A. C. Hatch, J. S. Fisher, A. R. Tovar, A. T. Hsieh, R. Lin, S. L. Pentoney, D. L. Yang and A. P. Lee, *Lab Chip*, 2011, **11**, 3838–3845.
- 26 P. V. C. Hough, US3069654A, United States, 1962.
- 27 Y. He, J. Yin, W. Wu, H. Liang, F. Zhu, Y. Mu, H. Fan and T. Zhang, *Anal. Chem.*, 2020, **92**, 8530–8535.